Received: 2 June 2021 | Revised: 12 July 2021 | Accepted: 19 July 2021

DOI: 10.1002/ces2.10102

International Journal of Ceramic Engineering & Science

RESEARCH ARTICLE

Crystallographic phase formation of iron oxide particles produced from iron nitrate by liquid flame spray with a dual oxygen flow

Miika Sorvali[1] | **Mari Honkanen**[2] | **Leo Hyvärinen**[3] | **Ritva Kuisma**[4] | **Jussi Larjo**[5] | **Jyrki M. Mäkelä**[1]

[1]Aerosol Physics Laboratory, Physics Unit, Faculty of Engineering and Natural Sciences, Tampere University, Tampere, Finland

[2]Tampere Microscopy Center, Tampere University, Tampere, Finland

[3]Engineering Materials Science, Materials Science and Environmental Engineering Unit, Faculty of Engineering and Natural Sciences, Tampere University, Tampere, Finland

[4]Research Center Terra, Tampere University, Tampere, Finland

[5]Oseir Ltd, Tampere, Finland

Correspondence
Miika Sorvali, Aerosol Physics Laboratory, Physics Unit, Faculty of Engineering and Natural Sciences, Tampere University, P.O. Box 692, FI-33014 Tampere, Finland.
Email: miika.sorvali@tuni.fi

Funding information
TUT/TAU Graduate school

Abstract

We fabricated iron oxide particles from iron(III) nitrate in a liquid flame spray synthesis. Unlike in most liquid flame spray studies, we implemented a secondary oxygen flow. The effect of the gas flow setup and two additives to the precursor solution, oxalic acid and citric acid, on the resulting particles was studied, with the focus on crystallographic phase composition. The synthesis yielded either pure maghemite or maghemite/hematite mixed phase powders. For solutions without additives, the maghemite fraction was almost linearly dependent on the equivalence ratio. The specific surface area was highest for the smallest equivalence ratios, then decreased, and increased again for the highest values. Some variation was observed between samples with equal equivalence ratios but the total oxygen flow divided differently between the two oxygen channels, a higher atomization flow promoting larger hematite fraction, and higher specific surface area. Both additives reduced the amount of hematite in the powder samples, citric acid being the more efficient one. Citric acid slightly raised the specific surface area, whereas oxalic acid dropped it in half.

KEYWORDS

iron oxide, liquid flame spray, nanoparticles, synthesis

1 | INTRODUCTION

Iron oxide is among the most relevant nanomaterials nowadays. It is special in the sense that it occurs in different crystallographic phases that manifest their own properties. Iron oxide particles are utilized in applications like biomedicine,[1,2] magnetorheological fluids,[3,4] and magnetic resonance imaging[5,6] in the two strongly magnetic phases, magnetite (Fe_3O_4) and maghemite (γ-Fe_2O_3), and in gas sensors,[7,8] catalysts,[9,10] and lithium-ion batteries[11,12] in the antiferromagnetic hematite (α-Fe_2O_3) phase. Other phases, whose potential has been less studied, also exist.[13,14] Because different phases, or even phase mixtures, provide varying functionalities, there is interest to develop methods that offer efficient synthesis with control over the phase composition.

Different synthesis methods offer their own advantages. Several chemical methods can provide careful

control of the particle properties, whereas simplicity, production speed, and upscalability are generally regarded as perks of flame methods. However, the fine tuning and the controllability of the end product is often challenging in a flame, where temperatures are high and time scales extremely short. Liquid flame spray (LFS), a specific type of flame spray pyrolysis (FSP) method, is in the focus of this article. Due to the difficulty of studying the very early stages of particle formation in flame synthesis, more experimental research is required to discover all the contributing factors. One of the still unclear parts of the process is the formation mechanisms of different phases and the factors that determine the eventual phase composition. Our goal is to shed a little more light into these processes through a specific experimental setup.

This study aims to build on the previous paper by Sorvali et al[15] that focused on factors affecting the phase of iron oxide nanoparticles produced in an LFS synthesis from iron(III) nitrate. The two main factors studied in the previous study were as follows: (a) the equivalence ratio (φ), controlled through adjusting O_2 and H_2 gas flows, when using pure alcohols as solvents, and (b) substituting part of the alcohol with a carboxylic acid in the precursor solution. The material primarily consisted of maghemite and hematite. φ, meaning the amount of substance ratio between the oxygen fed to the flame compared to stoichiometric combustion conditions, was observed to have a strong correlation with the maghemite/hematite ratio. However, when part of the alcoholic solvent was replaced with carboxylic acid, the hematite phase disappeared, and the amount added had an impact on the particle size distribution.

Here, we switched the burner to another design that allowed more flexible adjustment of the gas flows, thereby reaching lower equivalence ratios by enabling higher amounts of oxygen to be fed into the flame zone. Since the burner offered more complex flow mechanics, the effect of varying the flow setup was also inspected. In addition, we explored the effect of dissolving citric acid (CitA) or oxalic acid (OxA) as an additive to the precursor solution. The hypothesis was that these additives could cause the formation of citrate and oxalate complexes in the flame as intermediate species, changing the reaction pathways and possibly impacting the phase composition analogously to the assumed effect for carboxylic acid.

2 | EXPERIMENTAL

2.1 | Materials

The precursor used was iron(III) nitrate nonahydrate (FeN) ($Fe(NO_3)_3{\cdot}9H_2O$, 98+% (metals basis), Alfa Aesar). The solvents and the additives used were methanol (MeOH; EMSURE® ACS, Reag. Ph Eur, Merck), ethanol (EtOH) (99.5+%, Altia Oyj), citric acid monohydrate (99.5+%, Tamro Oyj), and oxalic acid (98%, Alfa Aesar).

2.2 | Nanoparticle synthesis

All samples were produced with LFS, whose basic principles are described in the literature.[16–18] Traditionally in LFS, a single hydrogen flow and a single oxygen flow are used to produce a turbulent H_2/O_2 flame, whereinto a liquid precursor solution is atomized with one of the two gas flows. Most of the published research utilizing LFS has been conducted in this sort of a setup and a burner with only two gas channels. However, we chose another burner design (earlier referred to as KP burner by Aromaa et al[16]) that has been used in a few recent studies.[19–22] With this burner, a small additional nitrogen flow is often added between the other flows to push the flame further from the burner head, thus keeping it clean.[16] We substituted this nitrogen flow with a secondary oxygen flow.

The burner has four gas channels as depicted in Figure 1, which makes adjusting the process more flexible compared to the other burner design with only two channels. With a single flow, there came a point when the pressure drop grew too large to increase the flow further, so the only way to raise the amount of oxygen in the flame zone (in an atmospheric synthesis process) was through an addition of a secondary oxygen flow. The choice of the specific gas flow setup will be addressed in the Results and discussion section.

The atomizing O_2 flow rate was varied between 5 and 15 slpm, and the secondary O_2 flow was between 5 and 60 slpm. The H_2 flow was fixed at 10 slpm, so we will be referring to the atomizing oxygen flow rate and the total oxygen flow rate simply by atomization flow (Q_{at}) and total flow (Q_{tot}). The iron nitrate precursor concentration was 0.54 M, which translates to 30 mg of Fe atoms per ml of precursor solution. The concentration was slightly lowered

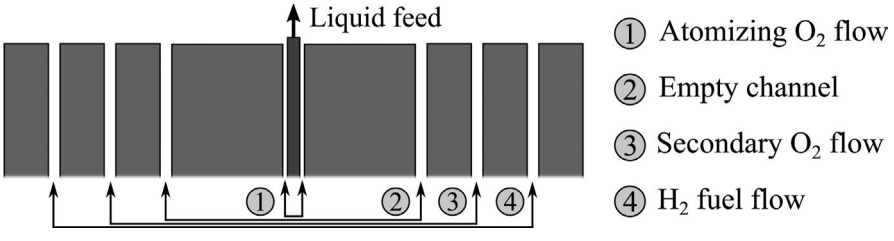

FIGURE 1 A schematic of the burner head and the gas flow setup used in the synthesis

from the previous study to ensure complete solubility of all species in every precursor solution. The precursor solution feed rate was fixed at 2 ml/min, so Q_{tot} was the variable that practically defined the equivalence ratio in each case. For CitA and OxA samples, the additive was dissolved in the precursor solution after the dissolution of iron nitrate in methanol. The samples were collected as a powder with an electrostatic precipitator described by Sorvali et al.[15]

2.3 | Atomization measurements

The atomization measurements were performed with a HiWatch HR2 instrument from Oseir Ltd. The instrument utilizes localized extinction of a multi-pulse laser beam for particle detection. Extremely rapid stroboscopic backlight illumination is used to record spray cross-section images that are processed in order to calculate droplet diameter and velocity distributions, among other measures. The working principle is described in more detail by Koivuluoto et al.[23] The measurements were performed with an ethanol feed of 1, 2, and 4 ml/min into a single oxygen flow that was varied between 3 and 15 slpm. The lower cut size of diameter measurement was between 4 and 5 μm, because the instrument could not distinguish droplets smaller than that. Ethanol was chosen instead of methanol for safety reasons.

2.4 | Characterization and sample preparation

X-ray powder diffraction (XRD; Panalytical Empyrean, monochromatized CoK_α radiation) was used to characterize the crystal structures present in the samples. The phase compositions were calculated from the XRD data with Rietveld refinement by BRASS 2 program.[24] The crystal structure models used for iron oxide were obtained from American Mineralogist Crystal Structure Database (AMCSD) with the codes 0020585 for maghemite (space group Fd-3m) and 0000143 for hematite (space group R-3c), as in the previous study.[15]

Transmission electron microscope (TEM; JEOL JEM-F200) was utilized to image particles. The TEM samples were prepared by dispersing sample powders ultrasonically in ethanol and dipping a grid in the suspension. Braun-Emmett-Teller (BET) measurements were performed with Micromeritics FlowSorb III 2035/2310 in a single-point mode to assess the specific surface areas (SSA) of the sample powders. SSA describes the total surface area per mass unit (m^2/g). The values were calculated as averages of measurements from two distinct samples of each powder, which together amounted to around 10%–30% of the total powder volume. The measured samples were degassed in 200°C for 2 h.

3 | RESULTS AND DISCUSSION

3.1 | Iron nitrate in pure methanol

In the previous study,[15] methanol, ethanol, and isopropanol were used as solvents. Since the choice between the three had a relatively small effect on the phase composition, we chose methanol for this study, because it was observed to be the most effective in dissolving additives and provided the most stable solutions in the long term.

Determining a suitable gas flow setup required some experimentation. Since the burner has three gas channels in addition to the atomization channel, the secondary O_2 flow and the H_2 flow could be positioned in several ways (Figure 1). The secondary O_2 flow was placed in the third channel, since using channel 2 led to significant accumulation of material onto the burner head. This was most likely due to swirling flows directed toward the liquid channel. When it was placed further from the liquid channel, the swirls weakened, greatly decreasing the accumulation. Placing the hydrogen flow between the two oxygen flows also had a similar fouling effect than using channel 2 for oxygen. The burning would initiate earlier, again leading to material accumulation, so it was put in the outermost channel.

The starting point of this study was reaching for lower φ values than previously by modifying the setup to allow feeding higher amounts of oxygen into the flame zone. Due to the complex flow mechanics resulting from the additional O_2 flow, we also wanted to study how the division of the total flow between the two channels affects the process and the end product. In theory, adjusting the flow division should impact the local flame temperatures, turbulence, and the residence time of the particles in the flame.

We initially chose three different atomization flows (Q_{at} = 5, 10, 15 slpm) and total flows (Q_{tot} = 20, 35, 65 slpm). A total of 11 samples were produced: three samples per each total flow and atomization flow (3 × 3 samples), plus two extra samples (Q_{tot} = 45, 55 slpm) for the 10 slpm atomization flow. With this setup, a φ range of 0.10–0.33 was achieved, and therefore, we continued down from where we left off in the previous study (0.32–1.76). Figure 2 shows the calculated weight fraction of maghemite (the rest was hematite) as a function of φ, alongside the results from the previous study,[15] obtained with another burner design. The Rietveld plots and refinement parameters are presented in Figures S1–S4 and Table S1.

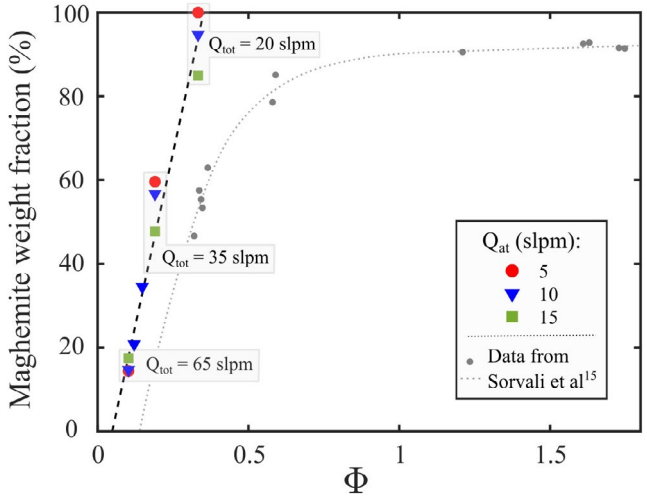

FIGURE 2 The maghemite fraction of the sample powders as a function of equivalence ratio. The results obtained in the previous study for another burner are plotted in grey for comparison. The total oxygen flows (Q_{tot}) are marked for the three φ values (0.10, 0.19 and 0.33), where Q_{at} was varied, but Q_{tot} kept constant

Just like before, the equivalence ratio had a strong correlation with the maghemite/hematite weight ratio. However, there are two clear differences to the previous results: the shape of the curve for higher equivalence ratios and the position of the curve on the φ axis. With the other burner, we covered a wide φ range. In the low end, the relationship seemed quite linear, but as we moved to an equivalence ratio of roughly 0.5, the curve started to flatten out, and eventually saturated at around 90% maghemite fraction. This saturation was hypothesized to be caused by oxygen diffusion from the surrounding air as the flame conditions became very anoxic. Now that we only moved in very low equivalence ratios, the relationship remained fairly linear for the whole range, and no saturation was observed. Maybe the additional oxygen flow helped keep the flame zone atmosphere better controlled.

Switching the burner and the flow setup surprisingly shifted the curve toward lower φ values. The same equivalence ratio of 0.32–0.33 that earlier produced around 50/50 phase ratio resulted in even pure maghemite (for $Q_{at} = 5$ slpm), which could not be reached at all with the other burner. This shift made a wider range of phase compositions available in both directions. If we assume that the 25% reduction in precursor concentration did not play a significant role here, the differing flow setup should be the reason for the discrepancy. The change in the experimental setup could lead to differences in the temperature field, which might be one of the key factors explaining the shift of the curve. Temperatures, in any case, are expected to decrease with φ, as the oxygen flow increases. Another difference separating this study from the previous one is the way φ was varied. The low φ range allowed it to be controlled simply by adjusting the oxygen flows, whereas the hydrogen flow needed to be changed in order to reach higher equivalence ratios. It would be interesting to experiment if the curve remained identical, if the equivalence ratio was controlled by adjusting the hydrogen flow also with this burner.

Even though the phase composition does not seem to be very sensitive to how the total flow is divided between the two oxygen channels, some differences in the phase composition among the three atomization flows are observable. For the 65 slpm total flow, the phase ratio was roughly the same for all three atomization flows, but the difference grew as the total flow was lowered. For the 35 and 20 slpm total flows, the highest atomization flow resulted in the highest amount of hematite. If a linear fit was made separately for each atomization flow, the slope would decrease with a growing atomization flow. Therefore, the correlation between φ and the phase ratio was slightly stronger for lower atomization flows.

We were also interested in other properties of the produced particles, so let us next take a look at how the SSA correlates with the phase composition. Figure 3 presents the BET results from two perspectives. Figure 3A portrays SSA as a function of Q_{tot} for different atomization flows and Figure 3B as a function of Q_{at} for different total flows.

The BET results are not straightforward to interpret against the Rietveld results. The SSA values varied between 29 and 87 m^2/g, which correspond to calculated average particle sizes of around 39 and 13 nm, respectively. The highest average SSA values were attained with the lowest total flow of 20 slpm. When Q_{tot} was increased to 35 slpm, the SSA dropped for every Q_{at}. We assume this to principally signal an increase in the residual particle volume. Simultaneously, a significant increase in the hematite fraction occurred. For the 10 slpm atomization flow, the SSA slightly decreases further with the raising of the secondary oxygen flow by 10 and 20 slpm, but much less dramatically compared to the first increment. However, for the highest total flow of 65 slpm, the SSA jumped up for all atomization flows. Since the hematite fraction grew continuously with increasing φ, SSA does not unequivocally correlate with it.

As Figure 3B exhibits, SSA values increased on average, when a larger portion of the total flow was shifted to the atomization channel. However, the 65 slpm total flow seems to be a special case also in this sense, since similarly to the hematite fraction, the SSA was practically independent of Q_{at}. For the two lower total flows, the higher hematite fraction correlated with a higher SSA.

Because the SSA strongly depends on particle morphology in addition to the size distribution, the BET results should be inspected in conjunction with TEM images. The particles could generally be divided into two modes: ultrafine primary particles (PP) and larger residual

particles (RP). The PP mode consisted of quite a narrow distribution of particles below 10 nm that covered most of the TEM sample areas, excluding the 65 slpm samples.

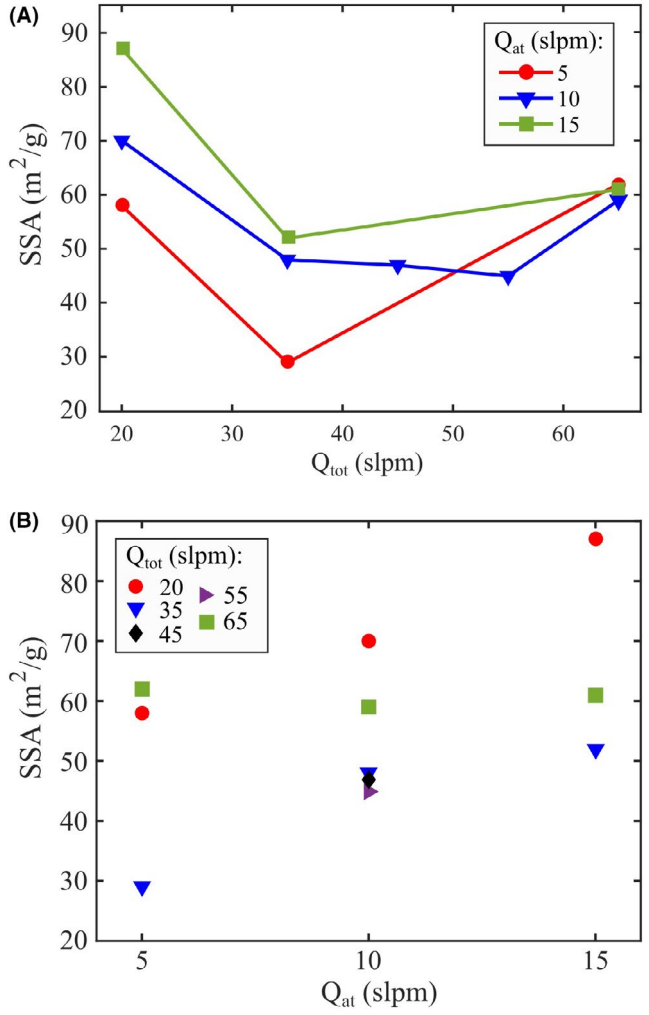

FIGURE 3 Specific surface areas as a function of (A) Q_{tot} and (B) Q_{at}

Figure 4 shows TEM images of PPs from 20 slpm samples as a function of atomization flow. The average particle sizes were calculated by picking random areas dominated by the PP mode and measuring all discernible particles, amounting to a few hundred particles per sample. The average PP sizes were not calculated for other samples, since the individual particles became too difficult to distinguish, especially for higher total flows. Some examples of these are presented in Figure S5.

The PP size for 20 slpm samples ranged mostly from 3 to 7 nm. As the atomization flow increased, the particle size decreased. A somewhat similar trend was observed for 35 slpm samples, which implies that a higher atomization flow promotes a smaller PP size. This variation in the average PP size is probably one of the main factors explaining the differences in SSA between the different atomization flows, depicted in Figure 3B. However, all the calculated BET particle sizes are clearly greater than those calculated for the PP mode, so all samples most likely contain residual particles.

The RP mode should have a more pronounced effect on the SSA compared to the PP mode, since large particles raise it even in relatively small numbers. We assume increasing the total flow from 20 to 35 slpm caused an increase in the RP mode volume, thus lowering the SSA values, but for the higher total flows, the situation becomes trickier. As total flow increased to 45 and 55 slpm, the SSA values still decreased slightly, but with 65 slpm, they jumped up. The relatively high SSA of around 60 m^2/g, which applied to every 65 slpm sample, implies that most of the powder would consist of primary particles. However, all the TEM images point to a different direction, as the sample areas were dominated by residual particles. Figure 5 shows some TEM images of samples with 10 slpm atomization flow. More TEM images of 65 slpm samples are shown in Figure S6.

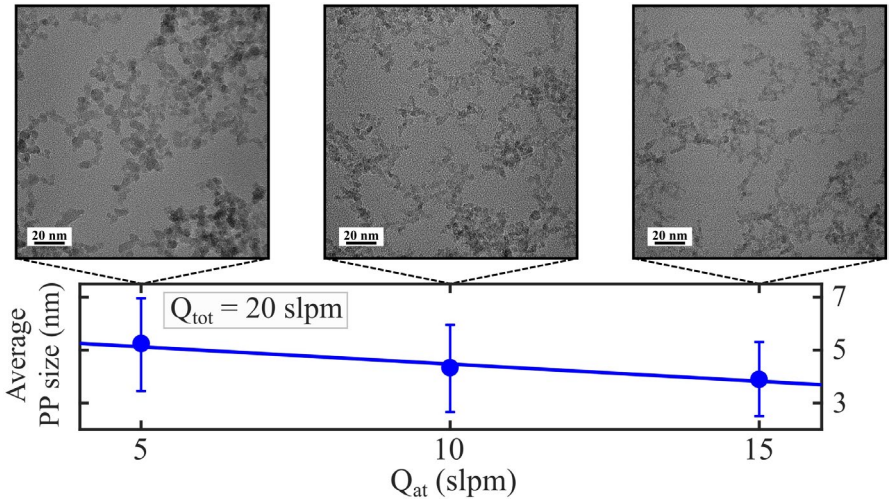

FIGURE 4 TEM images of primary particles from samples with total oxygen flow of 20 slpm. The average primary particles sizes were calculated arithmetically from a random area in the micrographs, and the error bars refer to standard deviations

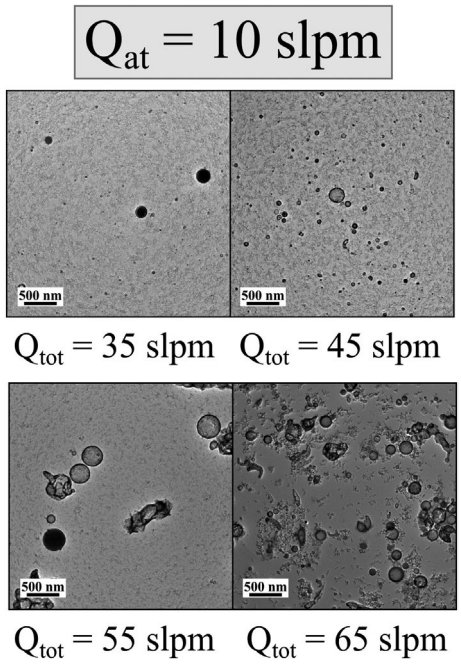

FIGURE 5 Transmission electron microscope images of residual particles in samples with 10 slpm atomization flow

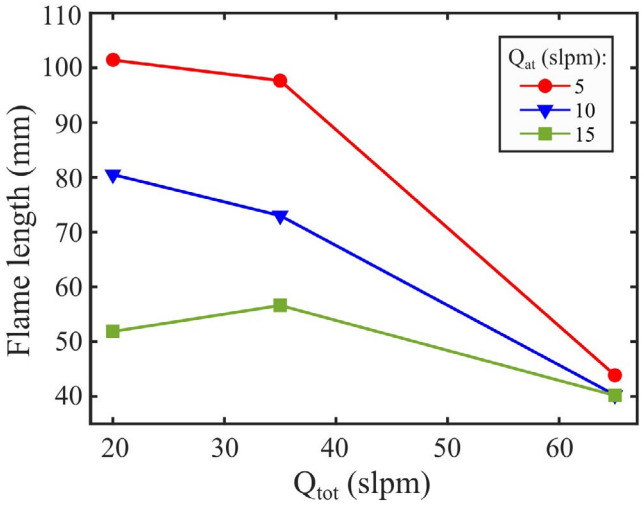

FIGURE 6 Flame length as a function of total flow for different atomization flows

It seems that as the total flow was raised, the number of irregularly shaped and hollow particles increased. Since hollow particles are often formed due to uneven evaporation, the temperature drop resulting from larger oxygen flow would understandably increase their number. For the 65 slpm samples, the PP mode seemed very scarce and hollow RPs dominated. We did not find many residual particles in the original 20 slpm TEM samples, but test samples heat-treated in 200 and 400°C revealed a RP mode with solid particles dominating (Figure S7). Presumably, the heat treatment should not have a great impact on the residual particle morphology. In other words, hollow particles remain hollow. We assume this increase of hollow particles to raise the SSA values, since hollow particles have a low effective density compared to solid particles. TEM imaging only covers a very small portion of the total sample volume, so this hypothesis cannot be completely verified. However, if this conclusion is correct, the hematite fraction could be more tightly linked to the number of hollow particles rather than residual particles, the PP mode consisting of primarily maghemite. This would also explain why no clear differences are observed between the widths of the XRD peaks corresponding to maghemite and hematite, because the shell of hollow particles could only contain relatively small crystallites.

To try to understand where the differences between the samples arise, we should examine the atomization and the flame structure. One of the main reasons for the discrepancies between the samples with the same total flow but differing atomization flows could emerge from the varying flame lengths. Even though the theoretical φ was constant, the flame length did not correlate with it linearly, as has been stated for FSP by Mädler et al.[25] This relationship seems to be very dependent on the experimental setup. Figure 6 shows the measured flame lengths for the three total flow combinations.

For the highest total flow, the flames were very short for all cases, which was expected in very oxic conditions. However, at lower total flows, the flame length became strongly dependent on the flow division. Growing atomization flow presumably increases turbulence in the flame zone, leading to flame contraction. The differences in average PP size observed between the different atomization flows probably stem from this phenomenon, since a shorter flame promotes a shorter residence time, and thus a lower PP size. Flame contraction also causes steeper temperature gradients compared to long flames. Short residence times and rapid quenching have been observed to be some of the governing factors in the phase formation of titanium oxide in FSP,[26,27] so they could promote hematite formation.

When estimating the residence time, the particle velocity also needs to be taken into account. We can use the atomization measurements to help examine the situation. Figure 7 shows the measured mean droplet velocities and diameters as a function of atomization flow for three different ethanol feed rates. The data point referring to droplet velocity at 1 ml/min feed rate and 3 slpm atomization flow was assumed to be a measurement error.

The droplet velocity behaved quite interestingly. With low atomization flows, the velocity increased as the flow was raised, but at around 6–7 slpm the velocity peaked, and the turbulence presumably started to take

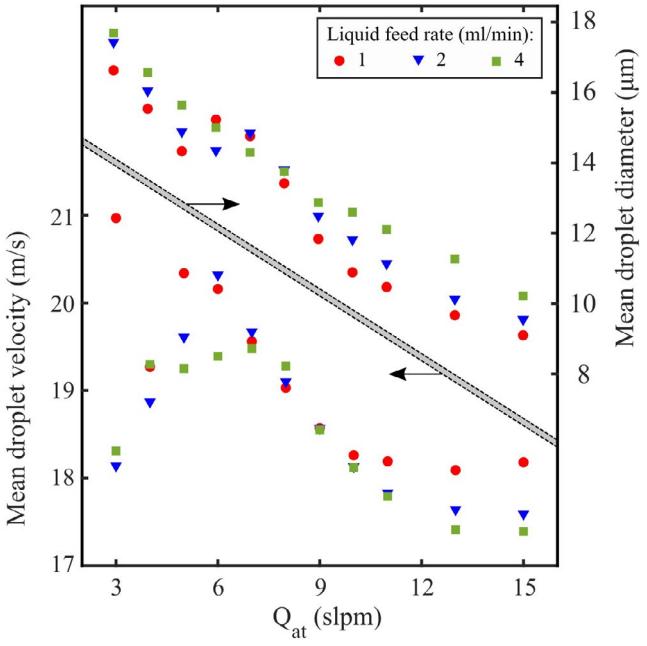

FIGURE 7 Measured mean droplet diameter and velocity as a function of Q_{at} for three different feed rates of ethanol. The graph is divided into two parts referring to different *y*-axes

over. From there on, the velocity decreased quite linearly until 12–13 slpm. This means that even though the velocity of the gas emerging from the burner head theoretically grows when the atomization flow increases, the residence time of the particles in the flame does not necessarily drop as dramatically. This might allow most of the precursor still to evaporate and form nanoparticles with 15 slpm atomization flow, although the flame is very short.

As expected, the mean droplet size decreased with the increasing atomization flow. The data points for the highest atomization flows are most likely a bit overestimated due to the 4–5 μm lower cut point of the instrument, since more sub-5 μm particles are generated. The decrease in average droplet size also means that the residual particles with 15 slpm atomization flow are likely smaller on average compared to the lower flow rates, which should also contribute to their highest SSA values.

3.2 | Addition of citric acid and oxalic acid

The effect of citric acid and oxalic acid as additives was studied by dissolving various amounts of them in the precursor solution, while keeping other parameters fixed. The "middle point" parameters of 10 slpm atomizing flow and 35 slpm total flow were chosen for all the samples. The additive-to-precursor ratios with respect to mass (R_m) and amount of substance (R_n) for different samples are presented in Table 1 with the calculated phase compositions and measured SSA values. Figure 8 shows the XRD patterns of the different samples with the most important peaks referring to maghemite (γ) and hematite (α) marked. The Rietveld plots and refinement parameters are presented in Figures S8 and S9 and Table S2.

Both additives dramatically decreased the amount of hematite that was otherwise formed. CitA was clearly the more efficient of the two additives in this respect, since 30% of the mass (around 60% of the amount of substance) of iron nitrate was adequate to eliminate basically the whole hematite phase, and already half of that amount erased most of it. Since no samples with lower amounts of CitA were prepared, we do not know how very small additions would behave. Much more OxA was required to eliminate the hematite phase, and even double the amount of substance compared to iron nitrate still left a noticeable (although barely) fraction in the sample. However, we are not aware whether a further increase in the amount of OxA would yield the same result as a lower amount of CitA. This difference could maybe be explained by inspecting the two molecules. CitA, having three carboxyl groups instead of two, and an additional OH group, would be assumed to have increased steric hindrance and be more prone to forming complexes than OxA. Therefore, a lower amount could provide the same effect.

The SSA results make an interesting distinction between the two additives. While the CitA addition, with all tested amounts, slightly increased the SSA, OxA addition dropped it to almost half of the additive-free precursor solution. There were no clearly observable differences in the PP size (shown in Figure S10), so the difference

TABLE 1 The additive-to-precursor ratios for mass (R_m) and amount of substance (R_n), the weight fractions of each phase, and SSA values for different samples with oxalic acid or citric acid as an additive.

Sample	R_m	R_n	Maghemite fraction (%)	Hematite fraction (%)	SSA (m^2/g)
Only MeOH	0	0	57.7	42.3	48
OxA 1	0.12	0.55	76.2	23.8	29
OxA 2	0.46	2.05	95.5	4.5	25
CitA 1	0.15	0.30	93.5	6.5	51
CitA 2	0.30	0.58	99.3	0.7	55
CitA 3	1.00	1.92	99.5	0.5	55

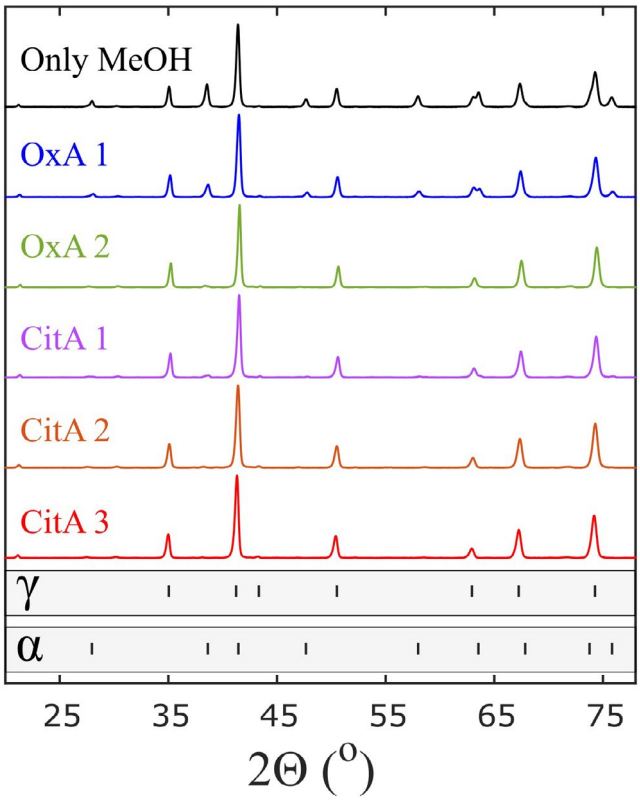

FIGURE 8 The XRD patterns of samples with the added oxalic acid or citric acid in the precursor solution. The growing number in the sample names refer to increasing amount of the additive. The main peaks of maghemite (γ) and hematite (α) are marked on the bottom

most likely comes from larger particles. One possibility is that there are more hollow residual particles in the sample without additives, and the OxA addition reduces their number, simultaneously increasing the number of solid residual particles. Another possibility could be an additional mid-sized particle mode that seemed to be especially prevalent in the OxA 2 sample (Figure S11). The TEM sample showed an evenly spread collection of nanoparticles in the size range of about 10–50 nm. The origin of these particles is unknown, but they could explain the drop in SSA. The different types of intermediate complexes formed by the two additives could also have an effect here.

The results for CitA and OxA cannot be directly compared to the results for carboxylic acid addition in the previous study,[15] because the experimental setup was different, and the precursor concentration a little bit higher. What makes the two situations somewhat comparable, though, is that the chosen parameters with pure methanol as the solvent produced very similar phase compositions in both cases (42.3% vs 44.6% of hematite). Already the lowest amount (5 vol-% of the solvent mixture) of added 2-ethyl hexanoic acid (EHA), which translates to R_m and R_n values of 0.13 and 0.36, caused a complete elimination of hematite. A further EHA addition seemed to reduce the RP mode, possibly due to the raised heat of combustion (HOC) of the precursor solution. EHA, as a solvent that has a significantly higher HOC than methanol, is a different type of additive compared to CitA and OxA that need to be dissolved and have lower HOC values per volume than methanol. The EHA substitution changed the particle distribution when increased in volume, while increasing the amount of CitA seemed to only have a very slight effect. Also, CitA can only be dissolved in limited amounts. On the positive side, it is quite a safe and readily accessible chemical, so it could be useful, if another way to eliminate residual particles would be discovered.

We are not aware of other flame synthesis studies performed with similar precursor solutions to ours, but there are some studies conducted with different synthesis methods from iron citrate, and also with CitA and OxA added to an iron precursor. In a reasonably low temperature (max 250°C) sol-gel synthesis, pure maghemite was obtained, when FeN-CitA mixture was used as the precursor.[28] A heat treatment of iron citrate at 500°C also resulted in pure maghemite.[29] The two studies that reported synthesis of pure hematite from FeN-CitA mixture, both had a calcination period of 4–6 h at 600°C in the end.[30,31] Since they performed no analyses before the calcination, we cannot be certain what kind of a phase composition was formed before it. Maghemite has been observed to transform into hematite at around 600°C.[32] Based on this literature, maghemite would likely be the more expected phase to be obtained with CitA, since LFS synthesis happens in a very short time period. However, chemical processes at high temperatures and short times are difficult to predict.

The results with OxA were more unexpected, because the literature we found on syntheses utilizing it resulted in hematite particles. Sol-gel and thermal decomposition syntheses from FeN-OxA mixtures have been performed at 400°C, resulting in pure hematite.[33,34] A chemical synthesis at 250–450°C from a FeN-OxA mixtures,[35] and thermolysis at 155°C,[36] both also resulted in pure hematite. These studies did not involve a calcination period at a high temperature, so a transformation from maghemite to hematite was very unlikely. Considering this literature, hematite would have been the more expected phase. The short times at high temperatures in flame synthesis, however, seem to change the process to yield mostly maghemite.

4 | CONCLUSIONS

We studied the underlying factors that determine the phase formation of iron oxide particles produced from iron nitrate in LFS synthesis. We continued from our previous paper[15] where another burner was used. The

previously used burner with a single oxygen flow and a single hydrogen flow was replaced with another burner that enabled adding a secondary oxygen flow between the atomizing flow and the hydrogen flow. This allowed us to explore how the process behaves in extremely low equivalence ratios (0.10–0.33), compared to what we studied before (0.32–1.76). We also studied how dividing the total oxygen flow differently between the two gas channels affected the iron oxide particles, when the equivalence ratio remained constant. The second part of the study focused on the effect of adding citric acid or oxalic acid to the precursor solution, while other parameters were kept constant. Phase control of iron oxide has previously been studied for at least atmospheric chemical vapor synthesis,[37] and FSP synthesis in a controlled atmosphere,[38,39] where the burner is in a somehow enclosed space, but not in an open flame synthesis process. The effect of using different precursor-solvent combinations on the phase composition of $Li_4Ti_5O_{12}$ in FSP synthesis has been studied.[40] Also, EHA has earlier been added to iron nitrate solution,[41] but not from the perspective of the phase composition.

All sample powders consisted of maghemite or a mixture of maghemite and hematite. The maghemite fraction correlated quite linearly with the equivalence ratio through the whole range, varying from around 14% to 100%. In the previous study, the maghemite fraction saturated at around 90% when φ was raised. The curve was also clearly shifted toward lower φ values compared to the results with the other burner. The equivalence ratio of ca. 0.32 that earlier resulted in roughly 50/50 phase ratio produced even pure maghemite. This indicates that the correlation between φ and the maghemite fraction is strongly dependent on the experimental setup. The specific surface area did not correlate with φ in a simple manner. The highest SSA values were obtained with the lowest φ, then decreasing, but jumping up for the highest φ. This phenomenon might have been connected to the residual particle morphology. The number of hollow particles seemed to increase with φ, which would explain relatively high SSA values for the largest total oxygen flow.

Some variation was observed between the samples with a constant equivalence ratio but differing oxygen flow division. A larger atomization flow promoted a higher hematite fraction and SSA. The higher SSA was likely connected to the decreasing primary particle size and the higher hematite fraction possibly to flame contraction. However, φ was still the main factor determining the phase composition.

Adding both oxalic acid and citric acid lowered the hematite fraction in the samples. Citric acid was more efficient than the two, requiring a smaller amount to produce pure maghemite. Oxalic acid addition significantly lowered the SSA compared to a pure methanol sample, whereas citric acid slightly increased it. The lowering of the SSA for oxalic acid was possibly due to the formation of a mid-sized particle mode in the size range of 10–50 nm.

We believe that this study provided valuable knowledge on the factors that govern phase formation of iron oxide particles in FSP synthesis, but a lot more research is needed to fully grasp the whole process. Especially, the nucleation mechanisms of different phases and the way the precursor chemistry affects the process remain far from complete understanding.

ACKNOWLEDGEMENTS

M. Sorvali wants to acknowledge the TUT graduate school for financial support. This work made use of Tampere Microscopy Center facilities at Tampere University.

ORCID

Miika Sorvali https://orcid.org/0000-0003-2697-4922

REFERENCES

1. Gupta AK, Gupta M. Synthesis and surface engineering of iron oxide nanoparticles for biomedical applications. Biomaterials. 2005;26:3995–4021.
2. Usov NA. Iron oxide nanoparticles for magnetic hyperthermia. SPIN. 2019;9(2):1940001.
3. Jönkkäri I, Sorvali M, Huhtinen H, Sarlin E, Salminen T, Haapanen J, et al. Characterization of bidisperse magnetorheological fluids utilizing maghemite (γ-Fe_2O_3) nanoparticles by flame spray pyrolysis. Smart Mater Struct. 2017;26(6):095004.
4. Kciuk M, Turczyn R. Properties and application of magnetorheological fluids. JAMME. 2006;18(1–2):127–30.
5. Laurent S, Forge D, Port M, Roch A, Robic C, Elst LV, et al. Magnetic iron oxide nanoparticles: synthesis, stabilization, vectorization, physicochemical characterizations, and biological applications. Chem Rev. 2008;108:2064–110.
6. Nosrati H, Salehiabar M, Fridoni M, Abdollahifar M-A, Manjili HK, Davaran S, et al. New insight about biocompatibility and biodegradability of iron oxide magnetic nanoparticles: stereological and in vivo MRI monitor. Sci Rep. 2019;9:7173.
7. Dutt M, Ratan A, Tomar M, Gupta V, Singh V. Mesoporous metal oxide–α-Fe_2O_3 nanocomposites for sensing formaldehyde and ethanol at room temperature. J Phys Chem Solids. 2020;145:109536.
8. Wei Q, Sun J, Song P, Yang Z, Wang Q. Metal-organic frameworks-derived porous α-Fe_2O_3 spindles decorated with Au nanoparticles for enhanced triethylamine gas-sensing performance. J Alloy Compd. 2020;831:154788.
9. Tamirat AG, Rick J, Bubale AA, Su W-N, Hwang B-J. Using hematite for photoelectrochemical water splitting: a review of current progress and challenges. Nanoscale Horiz. 2016;1:243–67.
10. Li S, Hu S, Xu K, Jiang W, Hu J, Liu J. Excellent visible-light photocatalytic activity of p-type Ag_2O coated n-type Fe_2O_3 microspheres. Mater Lett. 2017;188:368–71.

11. Zhu J, Lu Y, Chen C, Ge Y, Jasper S, Leary JD, et al. Porous one-dimensional carbon/iron oxide composite for rechargeable lithium-ion batteries with high and stable capacity. J Alloy Compd. 2016;672:79–85.
12. Narsimulu D, Nagaraju G, Sekhar SC, Ramulu B, Hussain SK, Yu JS. Unveiling multi-channelled 3D porous iron oxide nanostructures with exalted capacity towards high-performance Li-ion battery applications. J Alloy Compd. 2020;846:156385.
13. Brázda P, Kohout J, Bezdička P, Kmječ T. α-Fe_2O_3 versus β-Fe_2O_3: controlling the phase of the transformation product of ε-Fe_2O_3 in the Fe_2O_3/SiO_2 system. Cryst Growth Des. 2014;14:1039–46.
14. Sakurai S, Namai A, Hashimoto K, Ohkoshi S. First observation of phase transformation of all four Fe_2O_3 phases (γ → ε → β → α-Phase). J Am Chem Soc. 2009;131:18299–303.
15. Sorvali M, Nikka M, Juuti P, Honkanen M, Salminen T, Hyvärinen L, et al. Controlling the phase of iron oxide nanoparticles fabricated from iron(III) nitrate by liquid flame spray. Int J Ceramic Eng Sci. 2019;1:194–205.
16. Aromaa M, Keskinen H, Mäkelä JM. The effect of process parameters on the Liquid Flame Spray generated titania nanoparticles. Biomol Eng. 2007;24:543–8.
17. Mäkelä JM, Keskinen H, Forsblom T, Keskinen J. Generation of metal and metal oxide nanoparticles by liquid flame spray process. J Mater Sci. 2004;39:2783–8.
18. Mäkelä JM, Haapanen J, Harra J, Juuti P, Kujanpää S. Liquid Flame Spray – A Hydrogen-Oxygen Flame Based Method For Nanoparticle Synthesis And Functional Nanocoatings. KONA Powder Part J. 2017;34:141–54.
19. Brobbey KJ, Haapanen J, Tuominen M, Mäkelä J, Gunell M, Eerola E, et al. High-speed production of antibacterial fabrics using liquid flame spray. Text Res J. 2019;90(5–6):503–11.
20. Brobbey KJ, Haapanen J, Mäkelä JM, Gunell M, Eerola E, Rosqvist E, et al. Effect of plasma coating on antibacterial activity of silver nanoparticles. Thin Solid Films. 2019;672:75–82.
21. Juuti P, Nikka M, Gunell M, Eerola E, Saarinen JJ, Omori Y, et al. Fabrication of fiber filters with antibacterial properties for VOC and particle removal. Aerosol Air Qual Res. 2019;19:1892–9.
22. Temerov F, Pham K, Juuti P, Mäkelä JM, Grachova EV, Kumar S, et al. Silver-decorated TiO_2 inverse opal structure for visible light-induced photocatalytic degradation of organic pollutants and hydrogen evolution. ACS Appl Mater Interfaces. 2020;12:41200–10.
23. Koivuluoto H, Matikainen V, Larjo J, Vuoristo P. Novel online diagnostic analysis for in-flight particle properties in cold spraying. J Therm Spray Techn. 2018;27:423–32.
24. Fischer RX, Messner T, Kassner D. BRASS 2003: the Bremen rietveld analysis and structure suite. Z Kristallogr. 2006;15(1).
25. Mädler L, Stark WJ, Pratsinis SE. Flame-made ceria nanoparticles. J Mater Res. 2002;17(6):1356–62.
26. Manuputty MY, Dreyer JAH, Sheng Y, Bringley EJ, Botero ML, Akroyd J, et al. Polymorphism of nanocrystalline TiO_2 prepared in a stagnation flame: formation of the TiO_2-II phase. Chem Sci. 2019;10:1342–50.
27. Riad KB, Wood-Adams PM, Wegner K. Flame-made TiO_2(B). Mater Res Bull. 2018;106:276–81.
28. Kotsyubynsky V, Ostafiychuk B, Moklyak V, Hrubiak A. Synthesis, characterization and electrochemical properties of mesoporous maghemite γ-Fe_2O_3. Sol St Phen. 2015;230:120–6.
29. Mou F, Guan J-G, Shi W, Sun Z, Wang S. Oriented contraction: a facile nonequilibrium heat-treatment approach for fabrication of maghemite fiber-in-tube and tube-in-tube nanostructures. Langmuir. 2010;26(19):15580–5.
30. Habibi MH, Kiani N. Preparation of single-phase α-Fe(III) oxide nanoparticles by thermal decomposition. Influence of the precursor on properties. J Therm Anal Calorim. 2013;112:573–7.
31. Nandi AK, Pant A, Tripathi A, Newale SP, Gajbhiye VP, Jadhav AJ, et al. Large scale synthesis and characterization of α Fe_2O_3 nanoparticles for propellant applications. Proc of ICANMEET-2013. 2013:475–80.
32. Khan US, Amanullah, Manan A, Khan N, Mahmood A, Rahim A. Transformation mechanism of magnetite nanoparticles. Mater Sci-Poland. 2015;33(2):278–85.
33. Ba-Abbad MM, Takriff MS, Benamor A, Mohammad AW. Size and shape controlled of α-Fe_2O_3 nanoparticles prepared via sol–gel technique and their photocatalytic activity. J Sol-Gel Sci Technol. 2017;81:880–93.
34. Muruganandham M, Amutha R, Sathish M, Singh TS, Suri RPS, Sillanpää M. Facile fabrication of hierarchical α-Fe_2O_3: self-assembly and its magnetic and electrochemical properties. J Phys Chem C. 2011;115:18164–73.
35. Pant P, Naik BD, Ghosh NN. Synthesis of α-Fe_2O_3 nano powder by simple chemical method. Mater Technol. 2009;24(4):213–6.
36. Yatsenko DA, Pakharukova VP, Tsybulya SV, Matvienko AA, Sidel'nikov AA. Phase composition and structure of nanocrystalline products of solid-phase oxidative thermolysis of iron oxalate dihydrate. J Struct Chem. 2012;53(3):548–56.
37. Ruusunen J, Ihalainen M, Koponen T, Torvela T, Tenho M, Salonen J, et al. Controlled oxidation of iron nanoparticles in chemical vapour synthesis. J Nanopart Res. 2014;15:2270.
38. Strobel R, Pratsinis SE. Direct synthesis of maghemite, magnetite and wustite nanoparticles by flame spray pyrolysis. Adv Powder Tech. 2009;20:190–4.
39. Kumfer BM, Shinoda K, Jeyadevan B, Kennedy IM. Gas-phase flame synthesis and properties of magnetic iron oxide nanoparticles with reduced oxidation state. J Aerosol Sci. 2010;41:257–65.
40. Meierhofer F, Li H, Gockeln M, Kun R, Grieb T, Rosenauer A, et al. Screening precursor-solvent combinations for $Li_4Ti_5O_{12}$ energy storage material using flame spray pyrolysis. ACS Appl Mater Interfaces. 2017;9:37760–77.
41. Rosebrock CD, Wriedt T, Mädler L, Wegner K. The role of microexplosions in flame spray synthesis for homogeneous nanopowders from low-cost metal precursors. AIChE J. 2016;62(2):381–91.

SUPPORTING INFORMATION

Additional supporting information may be found online in the Supporting Information section.

How to cite this article: Sorvali M, Honkanen M, Hyvärinen L, Kuisma R, Larjo J, Mäkelä JM. Crystallographic phase formation of iron oxide particles produced from iron nitrate by liquid flame spray with a dual oxygen flow. Int J Ceramic Eng Sci. 2021;00:1–10. https://doi.org/10.1002/ces2.10102